

REPORT DOCUMENTATION PAGE

Form Approved
OMB No. 0704-0188

Public reporting burden for this collection of information is estimated to average 1 hour per response, including the time for reviewing instructions, searching data sources, gathering and maintaining the data needed, and completing and reviewing the collection of information. Send comments regarding this burden estimate or any other aspect of this collection of information, including suggestions for reducing this burden to Washington Headquarters Service, Directorate for Information Operations and Reports, 1215 Jefferson Davis Highway, Suite 1204, Arlington, VA 22202-4302, and to the Office of Management and Budget, Paperwork Reduction Project (0704-0188) Washington, DC 20503.

PLEASE DO NOT RETURN YOUR FORM TO THE ABOVE ADDRESS.

1. REPORT DATE (DD-MM-YYYY)		2. REPORT TYPE Final Technical Report		3. DATES COVERED (From - To) 1 Mar 2005 – 31 Dec 2007	
4. TITLE AND SUBTITLE Second Moment Closure Modeling of Complex Turbulent Flows				5a. CONTRACT NUMBER FA9550-05-1-0177	
				5b. GRANT NUMBER	
				5c. PROGRAM ELEMENT NUMBER	
6. AUTHOR(S) Dr. Sharath S. Girimaji				5d. PROJECT NUMBER	
				5e. TASK NUMBER	
				5f. WORK UNIT NUMBER	
7. PERFORMING ORGANIZATION NAME(S) AND ADDRESS(ES) Department of Aerospace Engineering Texas A&M University College Station TX 77843				8. PERFORMING ORGANIZATION REPORT NUMBER	
9. SPONSORING/MONITORING AGENCY NAME(S) AND ADDRESS(ES) Air Force Office of Scientific Research (AFOSR) 875 N. Arlington St., Rm. 3112 Arlington, VA 22203 <i>Rhett Jeffries/NA</i>				10. SPONSOR/MONITOR'S ACRONYM(S) AFOSR	
				11. SPONSORING/MONITORING AGENCY REPORT NUMBER	
12. DISTRIBUTION AVAILABILITY STATEMENT DISTRIBUTION A: Approved for public release; distribution unlimited.				AFRL-SR-AR-TR-08-0299	
13. SUPPLEMENTARY NOTES					
14. ABSTRACT Turbulence subject to unsteady forcing can exhibit novel features that cannot be explained using the well-known steady-turbulence paradigm. Modeling and prediction of such statistically unsteady flows are important in many practical AFOSR applications: turbine flows, wake-flows with vortex shedding, etc. Further, many flow control strategies depend upon the knowledge of unsteady turbulence dynamics to achieve the desired objectives. However, our understanding of unsteadily-forced turbulence dynamics or our ability to predict them is inadequate.					
15. SUBJECT TERMS					
16. SECURITY CLASSIFICATION OF:		17. LIMITATION OF ABSTRACT	18. NUMBER OF PAGES	19a. NAME OF RESPONSIBLE PERSON	
a. REPORT Unclassified	b. ABSTRACT Unclassified	c. THIS PAGE Unclassified	Unclassified	46	19b. TELEPHONE NUMBER (Include area code) (703)

SECOND MOMENT CLOSURE MODELING OF COMPLEX TURBULENT FLOWS

AFOSR GRANT NUMBER: FA9550-05-1-0177

Sharath S. Girimaji

Department of Aerospace Engineering
Texas A & M University, College Station, Texas 77843

Abstract

Turbulence subject to unsteady forcing can exhibit novel features that cannot be explained using the well-known steady-turbulence paradigm. Modeling and prediction of such statistically unsteady flows are important in many practical AFOSR applications: turbine flows, wake-flows with vortex shedding, etc. Further, many flow control strategies depend upon the knowledge of unsteady turbulence dynamics to achieve the desired objectives. However, our understanding of unsteadily-forced turbulence dynamics or our ability to predict them is inadequate. Unsteady forcing implies a mean velocity-gradient field that varies with time. Temporally varying mean-velocity gradient comprises of one or more of the following four fundamental forms of unsteadiness: 1) rotation of the eigen-directions of the mean strain rate tensor (with eigen values maintained constant); 2) temporal variation in the eigen values of the mean strain rate tensor (with eigen directions fixed); 3) rotation of the mean vorticity-vector axis (with vorticity magnitude maintained constant); and 4) temporal variation of the mean vorticity-vector magnitude (with the direction fixed). For example, homogeneous shear flow in a rotating reference frame, when considered in an inertial frame, is a combination of a mean strain-rate tensor with rotating eigen vectors (and constant eigen values) and a constant vorticity vector. In this project we undertook a systematic study of these various forms of unsteadiness. Two studies were completed and the results reported in two journal publications – in *Physics of Fluids* and *Journal of Fluid Mechanics*. Two other studies were initiated. All these efforts are detailed in this final report.

1 Introduction

Over the last several decades important progress has been made in our capability to model and predict steadily-forced turbulent flows with nearly rectilinear streamlines. The next engineering challenge is the modeling of turbulent flows subject to complicating influences such as unsteady forcing (due to external influences or internal instabilities), streamline curvature, frame-rotation and heat release. Many of the applications of interest to the Air Force involve flows in which turbulence is strongly modified by the above factors. It is well known that such flows can be best modeled in mathematically rigorous manner only at the level of second moment closure. The objective of the present research is two-fold: (i) perform direct numerical simulations (DNS) and rapid distortion theory (RDT) calculations of **unsteadily** forced turbulent flows to infer the behavior of pressure-strain correlation and other key turbulent processes; and (ii) develop pressure-strain correlation and other closure models which incorporate the requisite complex physics and are consistent with constraints based on the time-reversibility characteristics of the

Navier-Stokes equations. These constraints will serve specific purposes for enhancing the model capabilities in unsteady flows.

Over the last two decades, direct numerical simulations (DNS) and rapid distortion theory (RDT) have played a crucial role in providing important insight into fundamental turbulence processes leading to the development of improved closure models. However, much of this progress is restricted to turbulent flows subject to steady forcing. There are numerous turbulent flows of interest to the Air Force that are subject to time-dependent (unsteady) forcing: e.g., flows in turbines, internal combustion engines, vortex-shedding in wakes. Furthermore, there are many flow control strategies attempting to take advantage of unsteady turbulence dynamics to modify/control flow. Our understanding of fundamental turbulence processes in flows with rapidly varying mean flows is inadequate. To accumulate a reliable knowledge base on these flows, we must revisit many of the canonical flows and re-examine the turbulence features in the context of unsteady forcing.

Classification of unsteadiness. Detailed investigations of turbulence subject to unsteady forcing are relatively recent. Unsteady forcing implies a time-varying mean-velocity gradient which encompasses a very wide range of possibilities. Presumably, different types of unsteadiness can have vastly different effects on turbulence. This renders a systematic study of unsteadily-forced turbulence rather difficult. However, some progress can be made by recognizing that any arbitrary unsteadiness in the mean-velocity gradient can be expressed as a combination of four elementary forms of variations: 1) temporal changes in the eigen-values of the mean strain rate tensor, with eigen-directions fixed; 2) rotation of the eigen-directions of the mean strain rate tensor, with eigen-values maintained constant; 3) temporal changes of the mean vorticity-vector magnitude, with the direction fixed; and, 4) rotation of the mean vorticity-vector axis, with its magnitude maintained constant. Our ultimate goal is to study, in isolation, the effects of each type of unsteadiness on turbulence.

Studies performed during funding period. An idealized flow which has contributed greatly to our current understanding of steadily-forced turbulence is the homogeneous shear flow. We revisit this flow and study it in the context of unsteady forcing. Our objective is to perform DNS and RDT of homogeneous flows subject to periodic and rotating mean shear. The goal is to gain important insight into the various physical processes in statistically unsteady turbulent flows and evaluate the validity of current turbulent closures. We will then attempt to derive advanced second-moment closure models that can effectively simulate these effects. It is our expectation that these second moment closure models will serve as the starting point from which sophisticated subgrid stress closure models can be derived for high-resolution computations. Two studies have been completed and two others initiated during this funding period. We will detail these studies later.

Issues investigated. We address the following issues: (a) Effect of forcing frequency on the evolution of turbulence parameters such as kinetic energy, dissipation and Reynolds stress anisotropy; (b) Budgets of Reynolds stress and kinetic energy evolution; (c) Phase lag between applied mean strain and Reynolds stress; and (d) Comparison between DNS results and second moment closure models.

This project summary presents the most prominent results reported in two accepted journal articles:

1. Yu and Girimaji (2006) ‘DNS of homogeneous shear subject to periodic turbulence’. To appear in **Journal of Fluid Mechanics**.
2. Girimaji, O’Neil and Yu (2006) ‘Rapid distortion analysis of turbulence subject to rotating shear’. To appear in **Physics of Fluids**.

The reader is referred to these articles for more detailed results and discussions.

2 Periodic shear flow

The first flow is a homogeneous periodic shear flow where the mean velocity gradient is given by

$$\frac{\partial U_i}{\partial x_j}(t) = S_{max} \sin(\omega t) \delta_{i1} \delta_{j2}. \quad (1)$$

(We use the following notation: \mathbf{V} , \mathbf{U} and \mathbf{u} represent the total, mean and fluctuating velocity vectors) Thus, the mean-strain tensor has fixed eigen directions and temporally sinusoidal eigen values (elementary form 1 in the above list). In our DNS (direct numerical simulation) investigation, the desired velocity gradient is produced by introducing a body force which is a deterministic function of space and time. To sustain the initial homogeneous mean shear, a constant mean pressure gradient field is sufficient.

Governing Equations. To achieve time-varying shear flow, additional body force, $\mathbf{F}(\mathbf{x}, t)$, is required. For this purpose we will consider a body force that is a function of space and time, but completely deterministic: \mathbf{F} does not contain a fluctuating part. Now the mean and fluctuating velocity equations can be written as:

$$\frac{\partial U_i}{\partial t} + U_k \frac{\partial U_i}{\partial x_k} + \frac{\partial \langle u_i u_k \rangle}{\partial x_k} = -\frac{\partial \bar{P}}{\partial x_i} + F_i; \quad (2)$$

$$\frac{\partial u_i}{\partial t} + U_k \frac{\partial u_i}{\partial x_k} + \frac{\partial}{\partial x_k} (u_i u_k - \langle u_i u_k \rangle) = -\frac{\partial p'}{\partial x_i} - u_k \frac{\partial U_i}{\partial x_k} + \nu \frac{\partial^2 u_i}{\partial x_k \partial x_k}. \quad (3)$$

The fluctuating velocity and pressure field equations are unaffected by the forcing, provided the force is purely deterministic. The applied body force is

$$\mathbf{F} = \omega S_{max} (y - y_{ref}) \cos(\omega t) \vec{i}, \quad (4)$$

where \vec{i} is the unit vector along x -direction. Also, (x, y) correspond to (x_1, x_2) directions and y_{ref} is a reference point which we take to be at the center of the computational domain.

2.1 Results.

In this section, we will describe the observed results. Detailed analysis and explanations are provided in the next section. Figure 1 shows the evolution of the kinetic energy for various forcing frequencies over an extended period of time. It is clear that three types of responses are possible depending on the frequency of forcing. The three regimes are identified as low-, intermediate- and high-frequency regimes.

When the forcing frequency is low ($\Lambda/S \leq 0.14$), the evolution of the turbulent kinetic energy ultimately asymptotes to a constant value which is smaller than the initial value. At intermediate forcing frequencies (Λ/S is between 0.14 and 0.3), k increases at long times. At higher forcing frequencies ($\Lambda/S > 0.3$), the evolution of k shows a periodic variation, with the mean in the vicinity of initial value.

In Fig. 2, the kinetic energy evolutions of $\Lambda/S = 0.16$ case computed with three different wavenumber sets (of 6078, 13768 and 24318 discrete wavenumbers) are compared. The three plots are absolutely indistinguishable demonstrating that our results are not dependent on wave-number discretization. All the other results presented in this study employ 13768 discrete wave-numbers.

2.2 Low frequency Regime

Figure 3 shows the evolution of k in the low frequency regime. For steady shear ($\Lambda/S = 0$), k increases exponentially. At the lowest non-zero frequency ($\Lambda/S = 0.02$), k increases initially and, after reaching its maximum value, decreases monotonically to an asymptotic value. The same trend continues as frequency increases, with the initial peak and final asymptotic value decreasing progressively. At the highest frequency in this range, the kinetic energy is initially periodic with cycle-mean gradually declining. At later stages, it asymptotes monotonically to a small value. It appears that $\Lambda/S = 0$ case is a singular limit in the low frequency regime as the behavior at vanishingly small values is quite different.

Figure 4 shows the evolution of b_{11} . For steady shear ($\Lambda/S = 0$), b_{11} asymptotes to the maximum allowable value of $2/3$. This indicates that almost all of the kinetic energy in the steady forcing case is contained in the $\langle u_1 u_1 \rangle$ component. For non-zero frequencies, b_{11} and b_{22} (figure not shown) converge to $-1/3$. Thus, all of the kinetic energy is contained in $\langle u_3 u_3 \rangle$. Prior to the asymptotic stage, the evolution of b_{11} is different in the $\Lambda/S = 0.02$ and 0.14 cases. In the $\Lambda/S = 0.02$ case, b_{11} grows initially reaching a maximum, and then decreases monotonically to $-1/3$. In the $\Lambda/S = 0.14$ case, b_{11} decreases first, then oscillates with decreasing cycle-mean and asymptotes to $-1/3$ at a slower rate.

In Figure 5, for $\Lambda/S = 0$ we see that, as expected, P_{11} is always positive and grows with time. This leads to monotonic growth of kinetic energy at long times. For non-zero frequencies, the evolution of P_{11} is quite different. The production can be positive or negative at early times, but is mostly negative at later times and subsequently asymptotes to zero.

Figure 6 shows the evolution of the pressure-strain redistribution component Φ_{11} . In the zero-frequency (constant shear) and $\Lambda/S = 0.02$ cases, the pressure-strain correlation always removes energy from $\langle u_1 u_1 \rangle$. In the $\Lambda/S = 0.02$ case, there is a period of time ($5 \leq St \leq 10$) when both production and pressure-strain correlation are negative. In the $\Lambda/S = 0.14$ case, Φ_{11} always counters the effects of P_{11} . For all frequencies, Φ_{11} asymptotes to zero.

2.3 Intermediate frequency Regime

The evolution of the kinetic energy for the intermediate range of frequencies ($0.14 \leq \Lambda/S \leq 0.3$) is shown in Fig. 7. For all frequencies, k grows over long times. However, the growth patterns are not same for different frequencies. In the $\Lambda/S = 0.16$ case, k increases initially for a short time and decreases, apparently asymptoting to a lower value. Then, rather unexpectedly, at $St = 20$, k increases dramatically followed by a decline that negates some, but not all, of the gain. Then it appears steady for a period of time. Again, abruptly, the growth-decay-steady pattern reappears. In the $\Lambda/S = 0.20$ case, k varies periodically, and the cycle-mean increases slowly (compared to the $\Lambda/S = 0.16$ case) in time.

Figure 8 shows the evolution of b_{11} . We can see that b_{11} exhibits strong oscillations at both frequencies. In the $\Lambda/S = 0.16$ case, the average magnitude of b_{11} is larger than that in the $\Lambda/S = 0.20$ case, which reflects the different structure of anisotropy in the two cases. Both P_{11} and Φ_{11}/k also exhibit strong oscillations (Figs. 9 and 10). In these cases, Φ_{11} always counters the effects of P_{11} .

2.4 High Frequency Regime

At high frequencies ($\Lambda/S \geq 0.30$), turbulence statistics vary almost periodically as shown in the Figs. 11–14. The amplitude of the variation is smaller than those in low and intermediate regime. Within this range, the amplitude decreases as the forcing frequency goes up. The cycle-mean of k is slightly larger than its initial value, while the cycle-mean of b_{11} , P_{11} and Φ_{11} are all around zero. Clearly, the turbulence is close to its initial isotropic state at all times. Production and pressure-strain distribution appear to affect the velocity field very little.

2.5 Effects of the phase of forcing shear.

Thus far we have discussed the effects of forcing (shear) frequency on turbulence. Now, we will briefly discuss the effects of initial phase of the periodic shear. For any arbitrary initial phase that a new set of coordinates can be found in which only the (1,2) component of the mean velocity gradient tensor is non-zero. Since the fluctuating velocity field is initially isotropic, the coordinate transformation will not change the statistical description of the initial velocity fluctuations. Thus, all of the preceding results pertaining to turbulent kinetic energy and its production will be invariant to the initial phase of the periodic shear.

Before concluding this section, it is important to point out that, if the rapid pressure term is omitted from the calculations, the turbulent statistics vary purely periodically for all frequencies. Thus, all of the non-periodic features of the observed behavior at low and intermediate frequencies must be attributed to the effects of rapid pressure term. In the next section, we will attempt to understand and explain the role of rapid pressure-strain correlation.

2.6 Discussion

Many important aspects of rotating-shear RDT results presented in the previous section differ significantly from those of homogeneous shear flow in a rotating reference frame and of periodic shear flow (mean velocity gradient given by Eq. (1)). The most important difference is at small

unsteadiness frequencies. In the present case, at low forcing frequencies, the kinetic energy level declines and attains a steady state value that is smaller than the initial value. On the contrary, in the other two flows, asymptotic growth similar to the steady forcing case is observed. This growth rate, however, decreases with increasing unsteadiness frequency in both homogeneous shear in rotating reference frame and periodic shear (Eq. (1)) cases. Thus, the steady-forcing behavior is a natural limiting case of the vanishing unsteadiness frequency trend in those flows. In the present case, the steady-forcing behavior is distinctly different from the small frequency trend. At intermediate unsteadiness frequencies, turbulence grows in spurts in the present case. This type of sporadic growth pattern is not seen in other unsteady flows. The physical reasons for the growth and the intermittent manner in which it happens are unclear. On the other hand, the behavior at high forcing frequency is quite understandable. When the shear-rotation timescale is much smaller than that of turbulence evolution, production and rapid pressure-strain correlation process can only affect small perturbations on the initial field. We will now attempt to provide a qualitative explanation for the observed apparently aberrant behavior at low and intermediate frequencies.

Steady shear: To explain the observed behavior at this limit, we first recapitulate the RDT results of steady homogeneous shear (see also Pope text book: pp. 419-421). In the steady-forcing case, all unit wavenumber vectors evolve toward $(0, -1, 0)$ indicating that all vectors align along the negative 2-direction (see Eq. (10)). Then, as a consequence of continuity u_2 must vanish. The anisotropy tensor, at intermediate times ($St < 5$), approaches the two-componential state as $\langle u_2 u_2 \rangle$ vanishes. The $\langle u_3 u_3 \rangle$ component does not change significantly as it experiences no production. On the other hand, $\langle u_1 u_1 \rangle$ grows rapidly. At long times, turbulent fluctuations approach a one-componential state as the magnitude of $\langle u_1 u_1 \rangle$ vastly exceeds that of $\langle u_3 u_3 \rangle$. Thus, in general, the dominant effect of steady shear is to augment Reynolds stress component in the mean-flow direction ($\langle u_1 u_1 \rangle$ in this case) and suppress the component in the normal direction ($\langle u_2 u_2 \rangle$). The augmentation of the streamwise component is due to the effect of production and suppression of the flow-normal component is due to the action of pressure-strain correlation. We will now argue that this suppression of the flow-normal component is key to explaining the observed behavior.

Low forcing frequencies: Now let us consider the slowly rotating shear case. Initially, the orientation of shear is such that $\langle u_1 u_1 \rangle$ grows as seen from Fig. 4 and $\langle u_2 u_2 \rangle$ rapidly decreases (figure not shown). The decrease in $\langle u_2 u_2 \rangle$ is due to two factors. The negative production (that develops as shear rotates) contributes to some of the reduction and the rest is due to rapid pressure term as in the case of steady shear. During the intermediate stages of evolution, the shear rotates (at a rate dictated by Λ) to an orientation so that the velocity gradient tensor is of the form

$$\frac{\partial U_i}{\partial x_j} = \delta_{i2} \delta_{j1}. \quad (5)$$

The new orientation favors the growth of $\langle u_2 u_2 \rangle$ and reduction of $\langle u_1 u_1 \rangle$. If $\langle u_2 u_2 \rangle$ is driven to zero in the early stages before favorable shear alignment can augment it, then this component will remain zero at all subsequent times. This is due to the fact that favorable shear requires non-zero u_2 perturbation to produce $\langle u_2 u_2 \rangle$ component of kinetic energy. During this intermediate stage, the $\langle u_1 u_1 \rangle$ component which had previously experienced growth is quickly depleted by the action of pressure strain correlation. In the lowest frequency case, it is indeed driven to zero during this stage as seen from Fig. 4. At slightly higher frequencies, the depletion is

not complete in one cycle of shear rotation. If the alignment of shear changes before $\langle u_1 u_1 \rangle$ is completely depleted in the second quarter of the cycle, this component of stress will increase as it experiences favorable shear in the third quarter of rotation. Then, $\langle u_1 u_1 \rangle$ will alternately rise and fall, with depletion exceeding growth in each quarter cycle. Ultimately, the stress will vanish over several cycles of shear rotation as seen in $\Lambda/S = 0.14$ case in Fig. 4.

The role of rapid-pressure strain correlation can now be summarized as follows. This term depletes the Reynolds stress component in the flow normal direction: $\langle u_2 u_2 \rangle$ during the first and third quarter and $\langle u_1 u_1 \rangle$ during the second and fourth quarter of each shear rotation cycle. At low frequencies, the depletion is more complete than at high frequencies. It is this effect that leads to the observed behavior. Thus, in the absence of pressure-strain correlation, the Reynolds stress behavior will be quite different.

Intermediate forcing frequencies: As the frequency of rotation increases further ($0.14 \leq \Lambda/S \leq 0.16$), more of the stresses survive the depletion cycle due to rapid changes in the orientation of strain and consequently the action of pressure. Once in every few cycles, the shear aligns favorably with the existing fluctuations leading to the spurts of rapid growth. Following these periods of fast growth, the changing strain orientation leads to fairly steep decline due to the combined action of pressure-strain correlation and negative production. But the decline is not large enough to offset the growth, resulting in a net gain of kinetic energy after each growth-decline cycle. With increasing frequency, the growth spurts occur more frequently. However, the magnitude of growth diminishes as the requisite favorable alignment occurs for a shorter duration.

High forcing frequencies: When the forcing frequency is very high, the strain rate rotates too rapidly and production is not sustained for a long enough period for $\langle u_1 u_1 \rangle$ to grow. The rapid rotation also causes the pressure-strain correlation to change too quickly to suppress $\langle u_2 u_2 \rangle$ to any significant degree. As a result, the kinetic energy changes very little from its initial value.

Phase difference between mean strain tensor and Reynolds stress. The evolution equation for kinetic energy is

$$\frac{\partial k}{\partial t} = -2kb_{ij}S_{ij}. \quad (6)$$

The orientation between b_{ij} and S_{ij} is crucial in determining the evolution of k . It is the action of rapid pressure that creates the phase lag between the applied strain and Reynolds stress. Clearly, the phase lag will depend strongly on the shear rotation rate. For a given Λ/S , calculations show that the phase differences between b_{11} and S_{11} vary about a median value (α) as a function of time. It is this median value that is important for explaining the observed behavior as a function of forcing frequency. It is hard to directly compute this value from the data and we will surmise this indirectly from the sign and magnitude of production. Positive production will indicate favorable alignment ($\pi/2 < \alpha \leq \pi$). Negative production will indicate unfavorable alignment ($\pi/2 > \alpha \geq 0$).

1. In the constant shear case, the monotonic growth in production (Fig. 5) clearly indicates that the alignment between strain and stress is favorable ($\alpha \approx \pi$).
2. In the low non-zero frequency cases, the production is negative at long times indicating that the alignment is unfavorable ($\alpha \leq \pi/2$), consistent with the explanation provided earlier in this section.

3. The nearly periodic behavior of production at the intermediate frequencies (Fig. 9) shows that the phase difference is nearly $\pi/2$ but with occasional favorable alignment ($\alpha > \pi/2$) resulting in positive spikes in production as explained earlier in the section. While some negative excursions of production are also seen, the positive spurts outnumber the negative ones leading to overall positive production during these periods. On an average, in the intermediate regime, the alignment can be taken to be slightly favorable ($\alpha > \pi/2$).
4. At the highest frequencies, it is clear that the phase difference is $\alpha \approx \pi/2$ on an average, as no particular alignment is sustained for long enough time.

Simple mathematical model: Now we will attempt to construct a simple mathematical model that can mimic the observed range of behavior. Consider the scalar equation

$$\frac{\partial k}{\partial t} = -k \cos(t) \cos(t + \alpha) \quad (7)$$

In the equation, α is the phase lag and $\cos(t)$ and $\cos(t + \alpha)$ model b_{11} and S_{11} , respectively. Integrating the above model, we have the following evolution equation for the kinetic energy:

$$k(t) = e^{-\frac{1}{2}t \cos(\alpha) - \frac{1}{4} \sin(2t + \alpha) + \frac{1}{4} \sin(\alpha)} \quad (8)$$

Figure 15 shows the evolution of k using Eq. (8) for several values of α . We can clearly see that there are three different regimes of responses depending on value of α . For $\pi/2 < \alpha \leq \pi$, model- k evolution is very similar to that seen in the intermediate forcing regime. For $\alpha = \pi/2$, k is periodic and the RDT behavior in high frequency regime is recovered. When $\alpha < \pi/2$, k decays to zero. In the RDT case, at low forcing frequencies, k settles down to a constant value lower than unity. Thus, the turbulence responses to rotating shear can be explained qualitatively.

Summary of Study 1. The main findings are:

1. At low forcing frequencies, kinetic energy grows. At high frequencies, k decays. The critical frequency at which the asymptotic behavior changes from growth to decay is found to be around $\omega/S_{max}=0.5$. At very high frequency ($\omega/S_{max} = 10$), the periodically-forced turbulence behaves similar to decaying isotropic turbulence.
2. The observed behavior can be explained in terms of the stress-strain phase-lag ϕ at different forcing frequencies. The phase-lag goes from π at low frequencies to $\pi/2$ at high frequencies. Phase-lag of $\pi/2$ corresponds to no net production. Thus the production decreases progressively with increasing frequency. When the level of production falls below dissipation, turbulence cannot be sustained.
3. Normal anisotropy oscillates about non-zero asymptotic values in growth cases. In decay cases, the cycle-average of anisotropy appears to vanish at long time.
4. RDT does not capture the frequency-dependence of the asymptotic behavior. It predicts periodic k -behavior for all frequencies.

5. Second moment closures do capture the asymptotic frequency dependence, although the predicted critical value is smaller than that observed in DNS.
6. Comparison of RDT and DNS results appears to indicate that the onus is on the closure models for the non-linear terms to produce the observed asymptotic frequency dependence.

The next step is to develop second moment closures that do capture the behavior accurately.

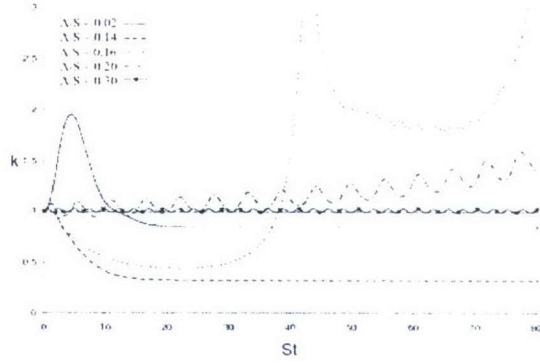


Figure 1: Extended kinetic energy evolution

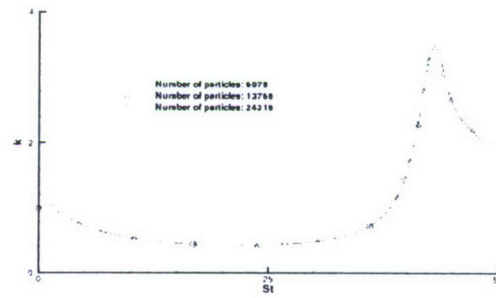


Figure 2: Kinetic energy evolution at various wavenumber discretizations: $\Lambda/S = 0.16$

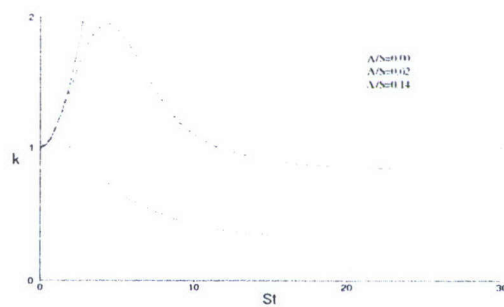


Figure 3: Low-frequency evolution of kinetic energy

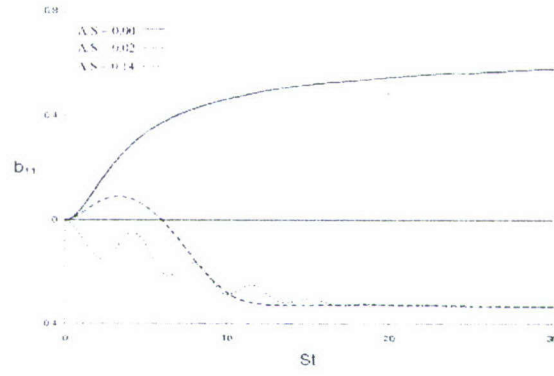


Figure 4: Low-frequency evolution of b_{11}

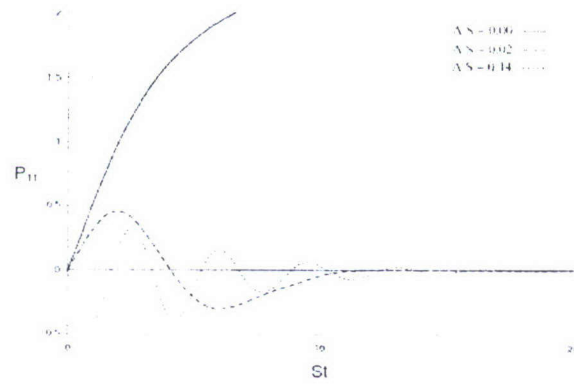


Figure 5: Low-frequency evolution of P_{11}

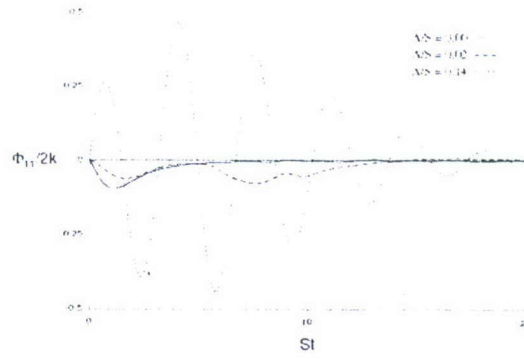


Figure 6: Low-frequency evolution of Φ_{11}

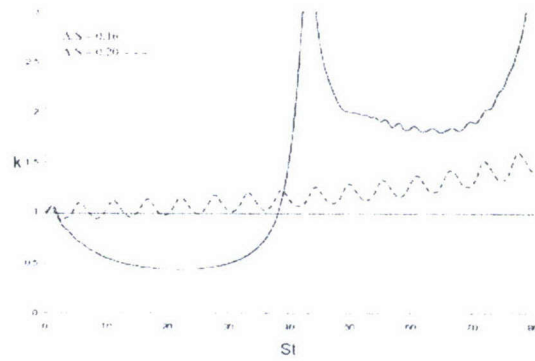


Figure 7: Intermediate-frequency evolution of kinetic energy

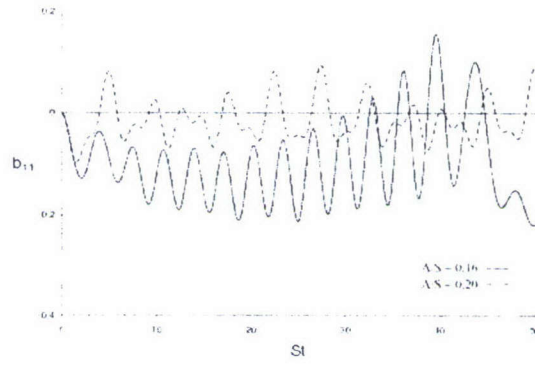


Figure 8: Intermediate-frequency evolution of b_{11}

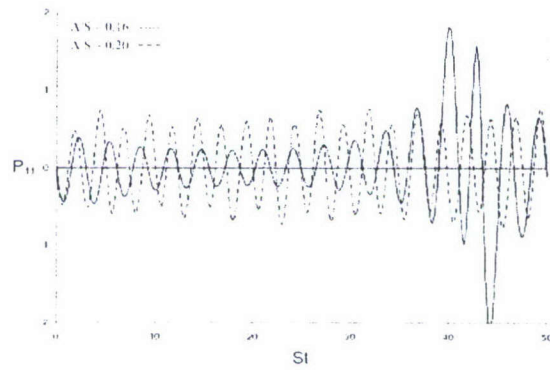


Figure 9: Intermediate-frequency evolution of P_{11}

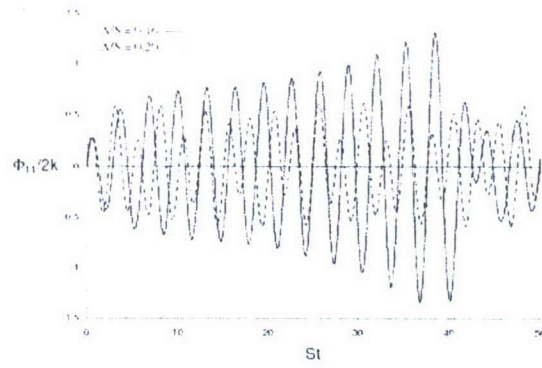


Figure 10: Intermediate-frequency evolution of Φ_{11}

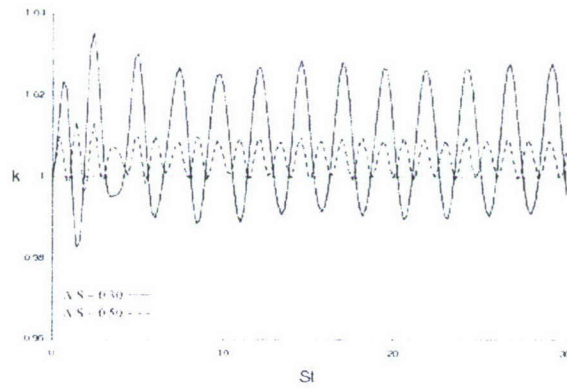


Figure 11: High-frequency evolution of kinetic energy

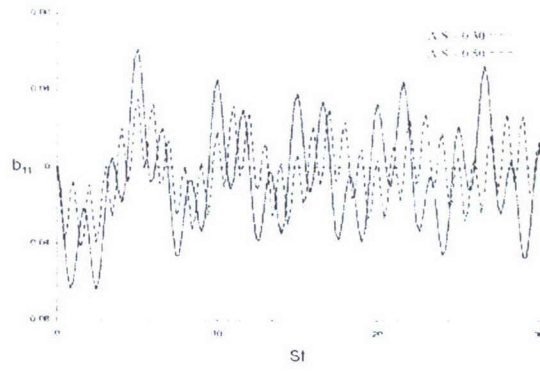


Figure 12: High-frequency evolution of b_{11}

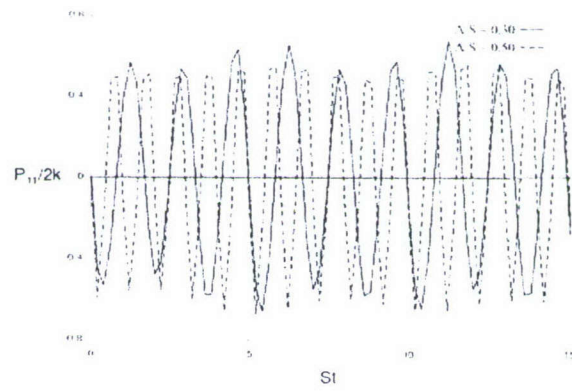


Figure 13: High-frequency evolution of P_{11}

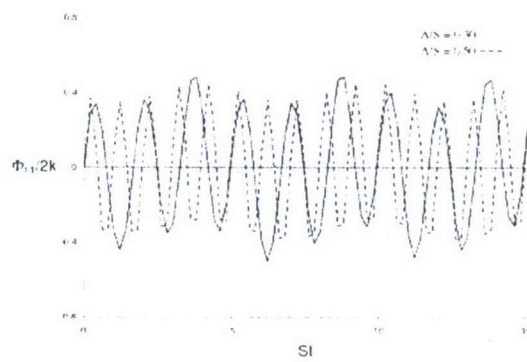


Figure 14: High-frequency evolution of Φ_{11}

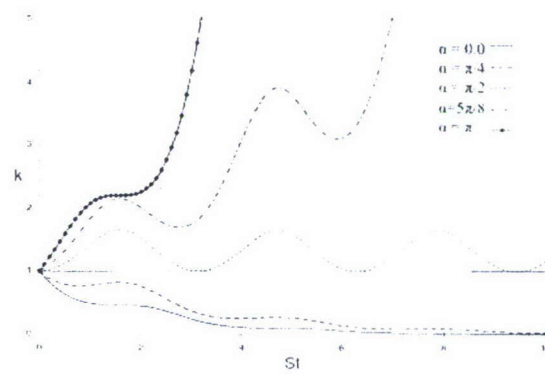


Figure 15: Evolution of k for various values of phase lag, α

3 Rotating Shear Flow

The second form of unsteady homogeneous shear which is being investigated in a concurrent study is a rotating shear flow:

$$\frac{\partial U_i}{\partial x_j}(t) = S \begin{bmatrix} \sin(2\pi\Lambda t)\cos(2\pi\Lambda t) & \cos^2(2\pi\Lambda t) & 0 \\ -\sin^2(2\pi\Lambda t) & -\sin(2\pi\Lambda t)\cos(2\pi\Lambda t) & 0 \\ 0 & 0 & 0 \end{bmatrix} \quad (9)$$

In this flow, the eigen values of the mean-strain rate tensor are constant but the eigen-directions rotate at a constant rate (elementary form 2). When the rotation rate is zero, the forcing reduces to a simple homogeneous shear. Again, the required time-varying velocity field is produced using a body force. Due to the basic difficulties in performing DNS of this flow, we will resort to RDT computations and restrict our considerations to linear processes. This type of unsteadiness is interesting for two reasons: (i) it is one of the four elementary forms of unsteadiness as discussed in the introduction; and (ii) the observed behavior as a function of frequency is remarkably different from that of other unsteady flows (periodic shear flows and homogeneous shear flow in rotating reference frame). Rotating homogeneous shear flow shares some common features with the homogeneous turbulence subject to periodic shear (elementary form 1) and rotating shear (elementary form 2). When considered in the inertial frame, it is clear that the eigen directions of the applied shear rotate and turbulence is subjected to time-dependent forcing. Rotating homogeneous shear flow has been the subject of many theoretical and computational studies. The major findings from these studies are: (a) for small rates of rotation (Ω) relative to shear S , turbulence grows in time, although slower than in the unrotated shear case; and, (b) for high rates of rotation, turbulent fluctuations become two-dimensional (as per Taylor-Proudman theorem) and turbulence decays rapidly. It is found that the observed behavior is well predicted by linear stability theory. Linear stability equations predict that turbulence can be sustained only for the range of parameter values $0 \leq |\Omega|/S \leq 0.5$. This range is very close to that observed in experiments and second-moment closure model calculations. We will examine if turbulence subject to rotating shear in an inertial reference frame exhibits similar behavior.

Governing Equations. The governing equations are most expeditiously solved in Fourier space (κ). The linearity of the governing equation at the RD limit permits the analysis of velocity ($\hat{\mathbf{u}}(\hat{\kappa}, \mathbf{t})$) and pressure ($\hat{p}(\hat{\kappa}, t)$) of each Fourier mode independently. The analysis is typically performed in a coordinate frame moving with the mean velocity. Thus the wave-number vector of a Fourier mode itself is a function of time, Pope (2000). It can be shown that the evolution equations for $\hat{\kappa}(\mathbf{t})$ and $\hat{\mathbf{u}}(\mathbf{t})$ are given by:

$$\frac{d\hat{\kappa}_l}{dt} = -\hat{\kappa}_j \frac{\partial U_j}{\partial x_l} \quad (10)$$

$$\frac{d\hat{u}_j}{dt} = -\hat{u}_k \frac{\partial U_l}{\partial x_k} \left(\delta_{jl} - 2 \frac{\hat{\kappa}_j \hat{\kappa}_l}{\hat{\kappa}^2} \right). \quad (11)$$

Note that these Fourier coefficients are further subject to the following incompressibility condition:

$$\hat{u}_i \kappa_i = 0. \quad (12)$$

The behavior of the velocity and pressure fields can be determined by simple integration over all wavenumbers. Summing this equation over all wavenumbers gives the evolution equation for the Reynolds stress in the RD limit:

$$\frac{\partial}{\partial t} \langle u_i u_j \rangle = -\langle u_j u_k \rangle \frac{\partial U_i}{\partial x_k} - \langle u_i u_k \rangle \frac{\partial U_j}{\partial x_k} + 2 \frac{\partial U_l}{\partial x_k} (M_{kjil} + M_{ikjl}) \quad (13)$$

where M_{ijkl} is a fourth order tensor defined by

$$M_{ijkl} = \sum_{\mathbf{k}^o} \hat{u}_i^* \hat{u}_j \hat{e}_k \hat{e}_l. \quad (14)$$

Turbulence production, P_{ij} is identified as

$$P_{ij} = -\langle u_j u_k \rangle \frac{\partial U_i}{\partial x_k} - \langle u_i u_k \rangle \frac{\partial U_j}{\partial x_k} \quad (15)$$

and the rapid pressure-rate-of-strain tensor $\Phi_{ij}^{(r)}$ is defined as

$$\Phi_{ij}^{(r)} = 2 \frac{\partial U_l}{\partial x_k} (M_{kjil} + M_{ikjl}). \quad (16)$$

Then Eq. (13) can be rewritten as

$$\frac{\partial}{\partial t} \langle u_i u_j \rangle = P_{ij} + \Phi_{ij}^{(r)}. \quad (17)$$

Thus, at the rapid distortion limit, Reynolds stress evolution is governed entirely by the linear processes of production and rapid pressure-strain correlation. The first step in performing the RDT simulation is to initialize the turbulence velocity field. In the present study, we consider an initially isotropic velocity field that is subsequently subjected to unsteady forcing.

3.1 DNS Results.

The effects of six different forcing frequencies on turbulence evolution are studied: $\omega/S_{max} = 0.125, 0.25, 0.50, 0.75, 1.0$ and 10 . In all the cases, the initial turbulence field is isotropic and prepared as described earlier and allowed to evolve. The various statistical moments are computed as a function of time. The results are sorted into several different categories: kinetic energy and dissipation; production; shear anisotropy; normal anisotropy; Reynolds stress budget; and, limiting high-frequency behavior. Each category is examined individually and in relation with other categories.

3.1.1 Evolution of k and ε

In all the cases studied, turbulence decays initially as the production is nearly zero (due to Reynolds stress isotropy) and dissipation is comparatively large. After the initial decay, subsequent evolution of k is different for different frequencies as shown in Fig. 24. In $\omega/S_{max}=0.125$ and 0.25 cases, k grows rapidly after the initial period of decay. The growth, however, is not

monotonic and cyclic variations from the mean trend is very much in evidence. In the case of $\omega/S=0.5$, the initial decay period is followed by a long duration of purely periodic behavior. Beyond $S_{max}t \approx 25$, the kinetic energy shows signs of very slow growth. In $\omega/S_{max}=0.75$ and 1.0 cases, k appears to decay with each cycle of applied strain. It is clear that two distinct turbulence responses are possible depending on the frequency of forcing. At low shear frequencies, turbulence grows at long times, although not necessarily monotonically. At high shear frequencies, turbulence decays. The switch from turbulence decay to growth occurs at a frequency of approximately $\omega/S_{max} = 0.5$. It is likely that at some normalized frequency close to 0.5 turbulence neither decays nor grows. It is however, difficult to precisely pin-point this value of frequency for which the turbulence level remains close to its initial condition. While the turbulence dynamics in the growth cases is likely to be similar to the steady forcing case, the physics of the decaying cases need further investigation.

Two decaying cases ($\omega/S_{max} = 0.5$ and 1.0) are studied in more detail next in Figs. 25 and 26. In these figures, the cycles of k variation are compared to those of S -variation and the behavior of dissipation is also examined. Clearly, the frequency of variation k is twice that of shear. We identify five points in time (A, B, C, D, and E) in one period (T_0) of shear cycle. Points A, C, and E correspond to consecutive zero-crossing times of S and points B and D correspond to the consecutive minima times in k variation. In $\omega/S_{max}=1.0$ case, consecutive k peaks have progressively smaller magnitudes indicating decay. In the $\omega/S_{max} = 0.5$ case, consecutive peaks in the intermediate period of evolution are nearly identical.

In all the cases considered, the evolution cycles of k and ϵ are in phase. This observation has important modeling implications. The current closure strategy of modeling production of dissipations in terms of production of kinetic energy appears to be valid for time-dependent forcing as well, at least at these low Reynolds numbers.

3.1.2 Time dependence of P/ϵ

A simple examination of the kinetic energy equation in homogeneous flows

$$\frac{dk}{dt} = P - \epsilon \quad (18)$$

reveals that k -evolution is completely dictated by the difference between production and dissipation. In order to understand the observed evolution of k , we investigate the behavior of P/ϵ ratio. This ratio must exceed unity for turbulence to grow.

Figures 27 and 28 show the evolution of P/ϵ . The evolution is generally oscillatory with periods of negative production. Negative production is rarely seen in turbulence subject to constant forcing but may be important in many practical flows. Over the first half-cycle of forcing, strain and production are in phase and their frequencies appear to be the same. However, a phase difference soon develops and the frequency of the ratio (P/ϵ) quickly becomes twice that of the applied strain as can be seen from monitoring the five reference points A, B, C, D and E (defined in Figs. 25 and 26). At all these points, production goes to zero. The zeros at A, C and E are due to the strain-rate going to zero. The zeros at B and D, it will be seen soon, are due to vanishing Reynolds stress component $\langle u_1 u_2 \rangle$. The frequency of the production cycle drives the kinetic energy cycle. Thus, the kinetic energy cycle is also twice that of the applied strain rate as seen previously. The cycle-averaged ratio grows gradually beyond unity in the low

frequency cases: $\omega/S_{max} \leq 0.5$. At higher frequencies, the cycle-averaged ratio lingers around zero (e.g., $\omega/S_{max} = 1$ case shown in Fig. 28). Thus, the observed k behavior can be completely explained in terms of the asymptotic trends of mean production-to-dissipation ratio.

3.1.3 Evolution of b_{12}

To gain further insight into the behavior of P/ε , we next examine the evolution of shear anisotropy b_{12} , which in conjunction with $S(t)$ determines production. In constant shear turbulence, b_{12} and S are of opposite signs.

The evolution of anisotropy component b_{12} in the $\omega/S_{max}=0.5$ case is shown in Fig. 29. The time variation of shear is also given in the figure. For the first quarter of the cycle, b_{12} is in phase with S and evolution is as expected. As the value of the applied strain begins to diminish after peaking, a phase lag develops. When the strain goes to zero at the half-cycle mark, the stress is clearly non-zero highlighting the hysteresis effect. For a substantial portion of the third quarter of the first cycle, stress and strain are of the same sign, implying that the production is now negative. Toward the end of the third quarter, the stress passes through zero and production becomes positive again. Throughout the fourth quarter of the first cycle, the stress and strain are of opposite signs. At the end of the first cycle, the stress does not return to zero. The phase-lag between stress and strain continues to grow for another cycle of applied strain. By the end of the second cycle, stress and strain lock into a constant phase difference and evolve at the same frequency. In this asymptotic state, the dynamics is again examined using the reference points A, B, C, D and E. We divide the A-E time period into four intervals: AB, BC, CD, and DE, as shown in Fig. 29. Just before time A, the shear is negative, b_{12} is positive, and production is positive. In the period AB, shear becomes positive while b_{12} still maintains positive values. In this period, production is negative as shown in Fig. 27. The negative production is also reflected in the rapid fall of k during the same period in Fig. 25. It can be seen in Fig. 29 that shear and b_{12} are relatively small in period AB hence the negative production is relatively small in magnitude. After time B, production returns to positive values until time C. As seen in Fig. 29, concurrence of large shear and b_{12} values produces large positive production during period BC. During period CD and DE, we see the same kind of production behavior as in periods AB and BC.

Figure 30 shows the evolution of b_{12} for $\omega/S_{max}=1.0$ case. The differences between the two cases are clearly evident. In $\omega/S_{max} = 1.0$ case, b_{12} is not initially symmetric about zero with the negative values being much larger than positive values. This is caused by the initial sign of the applied shear. In our simulation, the initial shear is positive leading to large initial negative values of b_{12} in the first half of the first cycle. At the second half of first cycle, the shear is negative and b_{12} is changing to positive values to keep in pace with the negative shear. However, before the b_{12} can reach its full potential magnitude on the positive side, the first cycle rapidly comes to an end and the applied shear is positive again. Thus, the positive excursions of b_{12} are not as large initially as the negative excursions. With the passage of time, the bias toward negative values decrease as the effect of the initial sign of applied shear fades and the oscillations become more symmetric. Calculations with initial negative shear show the opposite initial bias but do not change the observed asymptotic behavior of the evolution of kinetic energy, production and dissipation.

The difference between the low and high frequency cases at long times is more important.

Examining the time period A-E in the two cases, it can be seen that in $\omega/S_{max}=1.0$ case, period CD is much longer and period DE is much shorter than they are in $\omega/S_{max}=0.5$ case. This generates a large negative production during time CD and small positive production during time DE in $\omega/S_{max}=1.0$ case. Overall, the net production during a cycle can be judged by the lengths of AB+CD and BC+DE which correspond to the times when production has negative and positive values, respectively. If BC+DE is larger than AB+CD, net production will be positive. Otherwise, the cycle average of production will be negative. As b_{12} and S vary periodically, these lengths can be characterized by a single parameter: asymptotic phase lag (ϕ) between S and b_{12} . If $\pi/2 < \phi < \pi$, we will have $(BC+DE) > (AB+CD)$, and the net production will be positive. If, on the other hand, $0 < \phi < \pi/2$, we will have $(BC+DE) < (AB+CD)$, and the net production will be negative. If $\phi = \pi/2$, then $(BC+DE) = (AB+CD)$, resulting in no net production in a cycle of applied strain. For constant shear case, considering a constant shear as a pulse wave with infinite period, we have $\phi=\pi$. Thus the production will be always positive. In our computations, the phase difference between stress and strain vary initially, but lock into a constant value at latter times. The dependence of the lock-in phase-lag as a function of the applied frequency is shown in the original paper. It is seen that phase lag goes from nearly π in the very low frequency case to about $\pi/2$ in high frequency cases. Thus, the net production decreases with increasing frequency of forcing. It is curious to note that ϕ does not go below $\pi/2$ implying that net production is always non-negative. Thus, the net energy transfer in each cycle is from the mean to fluctuating field, except at very high frequencies at which the transfer goes to zero.

In order to sustain turbulence, the production must not only be positive, but must also exceed dissipation. From our computations, it appears that for $\omega/S_{max} > 0.5$, net cycle production is smaller than net cycle dissipation. We identify the critical frequency as $\omega_{cr} = 0.5S_{max}$, beyond which turbulence cannot be sustained. At higher frequencies, dissipation rate exceeds the rate at which energy is transferred from mean to fluctuating field.

3.1.4 Normal anisotropy

We now turn our attention to the normal components of Reynolds stress tensor. In inhomogeneous flows, these components play an important role in determining the secondary flow structures of the mean velocity field. The details of the evolution of the diagonal anisotropy components in $\omega/S_{max}=0.5$, 0.65 and 1.0 cases are given in Figs. 31, 32 and 33. The major observations and their implications are now summarized.

The frequency of all normal (or diagonal) anisotropies is the same as that of kinetic energy and twice that of the applied shear or off-diagonal (b_{12}) anisotropy. This is to be expected as the frequency of kinetic energy is also twice that of shear due to the influence of production. That the diagonal Reynolds stress component should have twice the frequency off-diagonal component can also be understood from a second point of view. Considering one cycle of the evolution of $\langle u_1 u_2 \rangle$, we can expect $\langle u_1 u_1 \rangle$ and $\langle u_2 u_2 \rangle$, which are always positive, to attain their maximum values during the maximum positive or maximum negative value of $\langle u_1 u_2 \rangle$. The diagonal Reynolds stress will attain their minimum value when $\langle u_1 u_2 \rangle$ crosses zero on its way from maximum to minimum value. Thus, in the time that it takes the off-diagonal component to complete a half-cycle from maximum to minimum through zero, the diagonal components complete a full cycle. The difference in frequency between the applied strain and diagonal

stresses also has important modeling implications. Approximations which imply that stress and strain have the same frequency will be invalid.

In the kinetic energy growth cases, the asymptotic cycle-mean anisotropy values are non-zero. For example, in the case of $\omega/S_{max} = 0.5$, the asymptotic cycle-mean values of b_{11} and b_{22} are about 0.15 and -0.1 respectively. In general, at all forcing frequencies, component b_{11} oscillates about a positive mean value and b_{22} about a negative value. The magnitude of the cycle-mean values of diagonal anisotropies decrease with increasing frequency. Thus, with increasing frequency, the diagonal stresses tend closer toward isotropic state. In all the decay cases, normal anisotropy tends to zero asymptotically, even if it develops non-zero values during first cycle of shear. Thus, the decay cases evolve asymptotically to isotropic turbulence.

3.1.5 Budget of Reynolds stress

Reynolds stress budgets offer more detailed insights into the physics of turbulence processes and are very important for high-order moment closure model development. We will now investigate the budgets of the various Reynolds stress components in the $\omega/S_{max} = 1.0$ case. Although the computations are performed with the lattice Boltzmann equation, the budgets will be discussed in the context of the Navier-Stokes equations. (The Reynolds stress budget equations are given in Section 3.) Following Pope (2000), production, pressure-strain correlation and dissipation are represented by P_{ij} , R_{ij} and ε_{ij} . Wherever possible, these budgets will be put in perspective with the budgets in constant shear homogeneous turbulence (Rogers 1986).

First and foremost, we must ensure that the numerical data is of high enough numerical fidelity that the various high-order derivatives and moments in the budgets can be computed with confidence. This is particularly important as the current computations employ novel LBM approach rather than the tried and tested Navier-Stokes schemes. Figure 34 shows the comparison of time derivative of Reynolds-stress $\langle u_1 u_2 \rangle$ computed from two independent means. One computation comes from summing the terms on the right hand side of Reynolds stress equation. The second estimate of the time-derivative comes from the finite difference operation on Reynolds-stress:

$$\frac{d \langle u_i u_j \rangle}{dt} = \frac{\langle u_i u_j(t + dt) \rangle - \langle u_i u_j(t - dt) \rangle}{2\delta t}.$$

The results from these two different computations are indistinguishable. Further tests were performed to ensure the fidelity of other budget-term calculations (figures not shown). The results clearly indicate that all terms in the Reynolds-stress budget equation are adequately accurate.

Figure 35 shows different terms in the budget of $\langle u_1 u_2 \rangle$ evolution. The magnitudes of the various terms diminish with time as k decays from its initial value. As is to be expected in the case of off-diagonal stress, dissipation is quite small at all times. The pressure-strain distribution always counters production and the difference between the two drives the evolution. This balance is very similar to that seen in the constant shear case (Rogers 1986), with the exception that production and pressure-strain distribution are now cyclic.

The budget of $\langle u_1 u_1 \rangle$ evolution is shown in Fig. 36. As in the case of constant shear, dissipation dominates the very early evolution ($S_{max}t \leq 1$) as the Reynolds stress value falls rapidly. Although zero initially, production becomes the most dominant term soon ($S_{max}t > 1$). Interestingly, the peak value of normalized production in the time-varying and constant shear

cases occur at the same normalized time: $S_{max}t = 2$. Pressure-strain redistribution almost always counters the effect of production, but there are rare instances when both the processes are of the same sign. It remains to be seen if the current pressure-strain redistribution closures can capture this behavior as most models assume that redistribution always counteracts production. At the intermediate stages ($1 \leq S_{max}t \leq 10$), the difference between production and the sum of dissipation and pressure-strain redistribution drives the evolution. At later stages, dissipation becomes negligible (in this decaying case).

The time dependence of budgets of $\langle u_2u_2 \rangle$ and $\langle u_3u_3 \rangle$ are quite similar and latter budget is shown in Fig. 37. For both components, production is absent. Dissipation dominates the initial time ($S_{max}t \leq 3$) development but quickly goes to zero thereafter. The later development is mainly due to pressure-strain redistribution. The production of $\langle u_1u_1 \rangle$ is the only source of kinetic energy in this flow. We see that the magnitudes of production, the dissipation and redistribution decrease with time. The increase of the magnitude of P/ε in Fig. 28 is caused by the faster decrease of ε , rather than the increase of P .

Overall, it is clear that pressure redistribution plays a key role in determining the evolution of various normal components. Calculations were performed to confirm that the trace of the pressure-strain redistribution was indeed close to zero. Analysis of the three components reveals that R_{11} and R_{22} are nearly in phase, while the phase of R_{33} is shifted nearly by π . This means that energy is removed from $\langle u_1u_1 \rangle$ and $\langle u_2u_2 \rangle$ and added to $\langle u_3u_3 \rangle$. This is different from what is observed in constant shear homogeneous flow. In the constant shear case, pressure-strain redistribution removes energy from $\langle u_1u_1 \rangle$ and augments $\langle u_2u_2 \rangle$ and $\langle u_3u_3 \rangle$. Closer examination of the constant shear budgets of Rogers (1986) reveals that the rapid pressure-strain redistribution does remove energy from both $\langle u_1u_1 \rangle$ and $\langle u_2u_2 \rangle$ and augments $\langle u_3u_3 \rangle$. It is the slow pressure-strain redistribution that is responsible for the augmentation of the $\langle u_2u_2 \rangle$ component. In the present time-varying shear case, we expect the non-linear slow term to be less dominant at later times as the turbulence decays quickly.

3.1.6 Limiting high-frequency behavior

As mentioned in the Introduction, the present flow shares some similarities with homogeneous shear flow in a rotating reference frame. For example, in both cases turbulence grows when the frequency (of rotation or periodic variation) is small and decays when the frequency is large. However, there are very significant differences in the turbulence dynamics in the two cases. In the case of homogeneous shear flow in a rotating reference frame, turbulence tends to a two-componential limit at large rotation rates in keeping with the Taylor-Proudman theorem. Two-dimensionalization inhibits cascade (no vortex stretching) and diminishes production leading to viscous decay of the velocity field at all scales. In the present case, on the other hand, turbulence is isotropic at large frequencies of shear variation. The shear varies too rapidly to induce anisotropy and produce kinetic energy. We anticipate that at high frequencies, turbulence subject to rapidly varying shear will be more like decaying isotropic turbulence as production will not be significant. To establish that this is indeed the case, we will now compare $\omega/S_{max}=10$ case with decaying isotropic turbulence.

In the decaying isotropic turbulence simulation, all the initial conditions are the same as for homogeneous shear flow, except that wall boundary condition is replaced by periodic boundary condition and there is no mean shear in the flow. Figure 38 shows the evolution of k and ε

for homogeneous shear and isotropic decaying cases. For consistency, time is normalized with S_{max} , although there is no shear in isotropic decaying turbulence. In homogeneous shear case, at initial stage, k decays a little bit slower than in isotropic decaying case. But over all, the decay rates are almost same for both cases. A similar examination of the dissipation rate demonstrates that the evolution in the two cases are almost indistinguishable. The standard power-law decay is recovered in both cases. It must be pointed out that there are about 15 shear cycles in the period over which the comparison is made.

Next we compare the evolution of anisotropy in the two cases in Fig. 39. The small level of anisotropy seen in the initial condition is due to finite statistical sample size. The time-development of the diagonal anisotropies in the decaying and high-frequency forcing cases are quite similar, with the latter exhibiting small-amplitude oscillations about the former. With regard to b_{12} , the difference between the two cases is quite discernible. The negative bias of b_{12} in the forced case has already been explained above. The most significant features are: the cycle-averaged b_{12} in the forced case is quite different from the b_{12} in the isotropic decaying case; and the amplitude of oscillation is quite sizable. Despite the large amplitude of b_{12} variation, the production is very small due to the fact that stress and strain are out of phase by $\pi/2$. Thus, the diagonal anisotropies, kinetic energy and dissipation are not very different from those in the unforced decaying case.

Thus, the limiting turbulence behavior in homogeneous shear flow in a rotating reference frame is dictated by Taylor-Proudman theorem and characterized by two-dimensional fluctuations. In the periodic shear case, the limiting behavior is characterized by statistically isotropic fluctuations and turbulence decays as in unforced case.

Summary of Study 2. The RDT results reveal that the turbulence response to this type of rotating shear is somewhat unexpected. We observe the following responses as a function of forcing frequency: (i) At low forcing frequencies ($0 < \Lambda/S \leq 0.14$), initially isotropic turbulence rapidly evolves to one-component state and kinetic energy asymptotes to a value smaller than the initial level. (ii) At intermediate frequencies ($0.14 < \Lambda/S \leq 0.20$), the turbulence kinetic energy exhibits sporadic spurts of growth. (iii) At larger frequencies, production and pressure-strain distribution perturb the field only slightly from its isotropic initial state. The sporadic growth observed at the intermediate forcing frequencies is quite unexpected. A qualitative explanation for the observed behavior is presented in the referenced paper. It is argued that the rapid pressure-strain correlation is responsible for this somewhat anomalous behavior. Although the physics of the observed behavior is quite complicated, we demonstrate that by simply accounting for the phase lag between stress and strain, the observed behavior can be approximately reproduced. A more quantitative explanation will require precise closure model for the rapid pressure-strain correlation. None of the current models come close to predicting the behavior observed in this paper. Development of closure models that can quantitatively capture the observed physics is the next step.

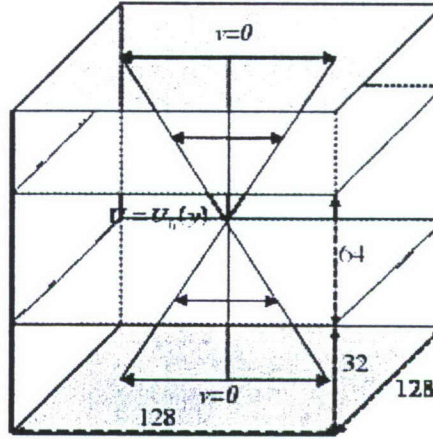


Figure 16: Computational domain. The statistics are obtained in the core region of computational domain which is $128 \times 64 \times 128$.

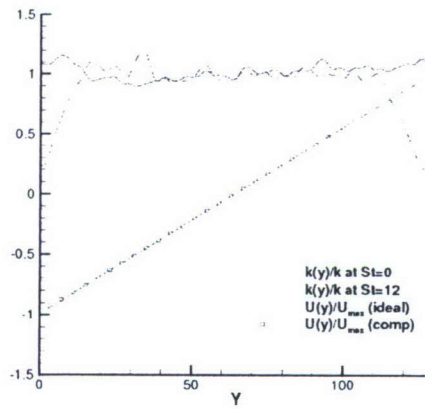


Figure 17: The profile of mean velocity at $St = 12$ and the distribution of $k(y)$ at initial stage and $St = 12$. The wall effects are limited to regions near the walls. In the inner region, mean velocity agree very well with the ideal mean velocity and homogeneity of turbulence is maintained.

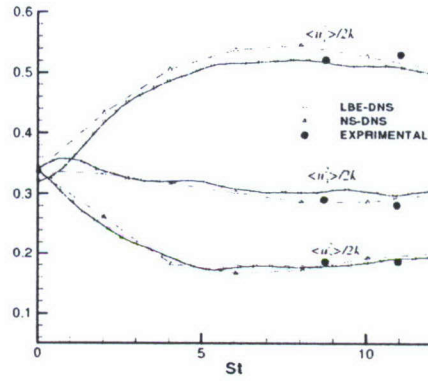


Figure 18: Evolution of normal Reynolds stress in homogeneous turbulent shear flow (constant shear). NS-DNS data are from Rogers (1986) with initial values of $Re_\lambda \approx 35$ and $S^* = 1.2$. Experimental data are from Tavoularis and Corrsin (1981a) with $Re_\lambda = 284$ at $St = 8.6$.

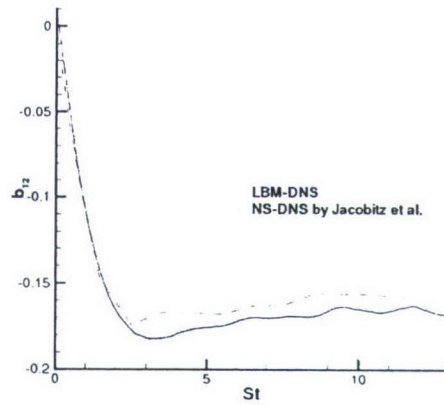


Figure 19: The results of b_{12} obtained from DNS using LBM and Navier-Stokes equations by Jacobitz, Sarkar & Van Atta (1997) with the initial values of $Re_\lambda = 44.72$ and $Sk/\varepsilon = 2.0$.

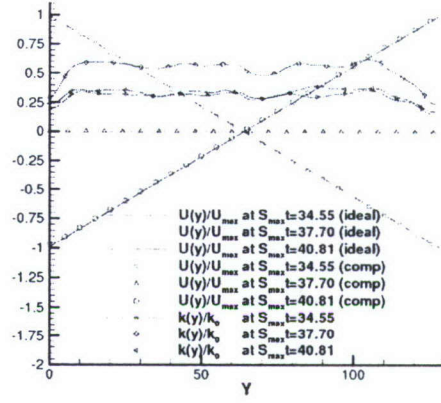


Figure 20: The profiles of $U(y)$ and $k(y)$ at $S_{max}t = 34.55, 37.70$, and 40.81 for $\omega/S_{max}=0.5$. Ideal vs. computed.

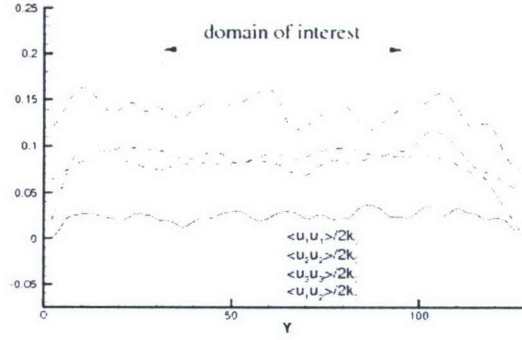


Figure 21: Planar-averaged Reynolds stresses along y -direction at $S_{max}t = 34.55$.

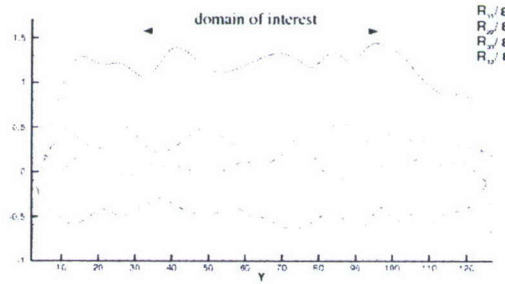


Figure 22: Planar-averaged Pressure-strain correlations along y -direction at $S_{max}t = 34.55$.

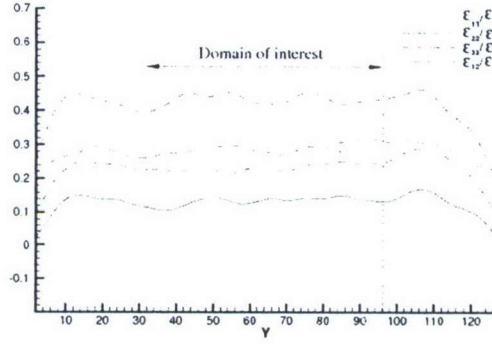


Figure 23: Planar-averaged components of dissipation tensor along y -direction at $S_{max}t = 34.55$.

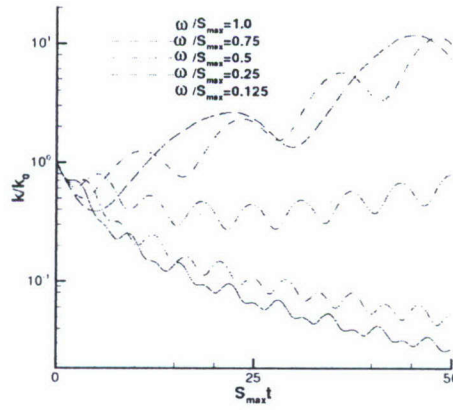


Figure 24: Evolution of k in various ω/S_{max} cases.

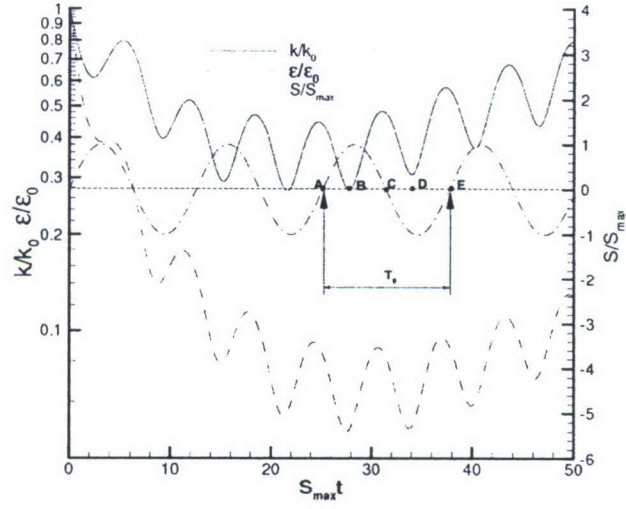


Figure 25: Evolution of k and ε in $\omega/S_{max} = 0.5$ case.

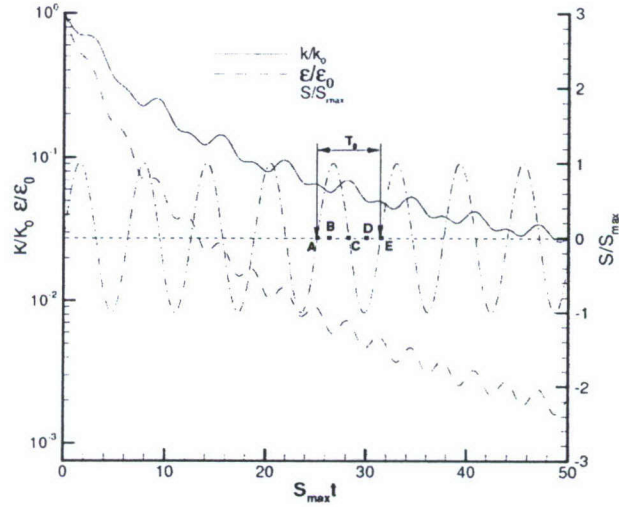


Figure 26: Evolution of k and ε in $\omega/S_{max} = 1.0$ case.

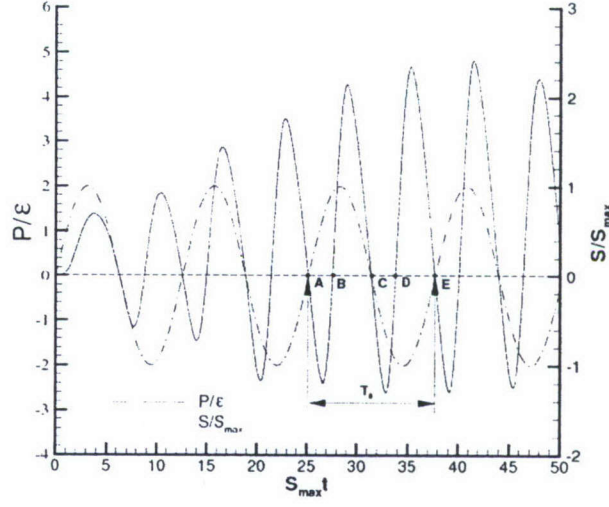


Figure 27: Evolution of production over dissipation ratio (P/ε) in $\omega/S_{max} = 0.5$ case.

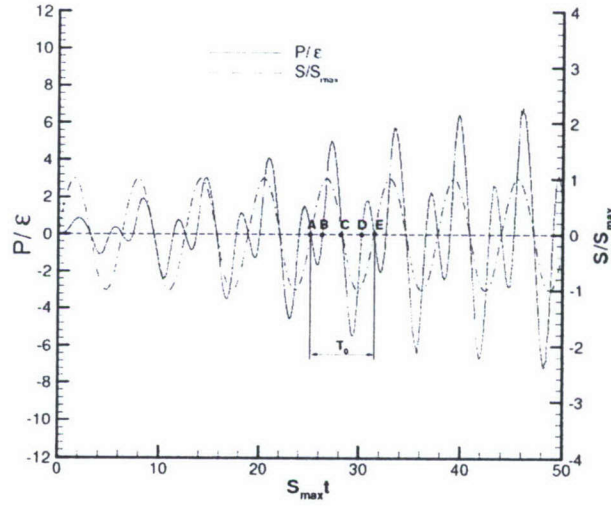


Figure 28: Evolution of production over dissipation ratio (P/ε) in $\omega/S_{max} = 1.0$ case.

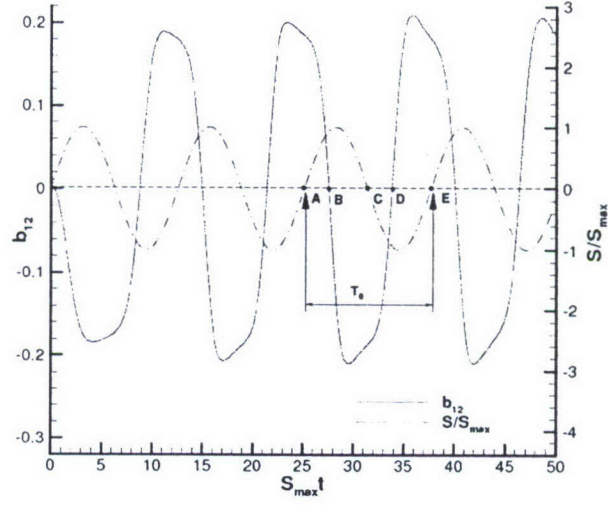


Figure 29: Evolution of b_{12} in $\omega/S_{max} = 0.5$ case.

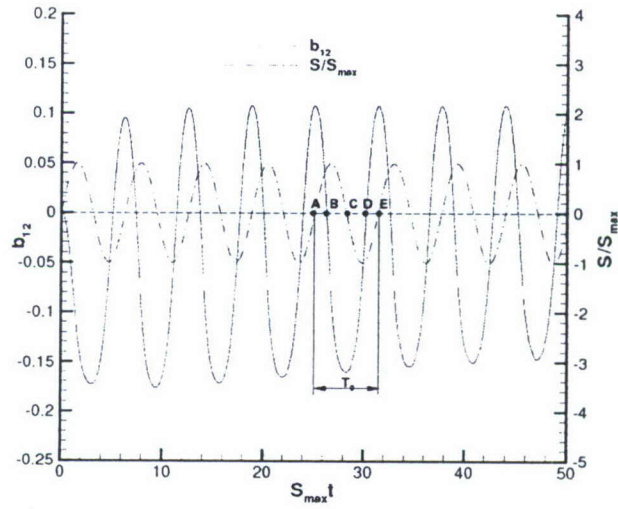


Figure 30: Evolution of b_{12} in $\omega/S_{max} = 1.0$ case.

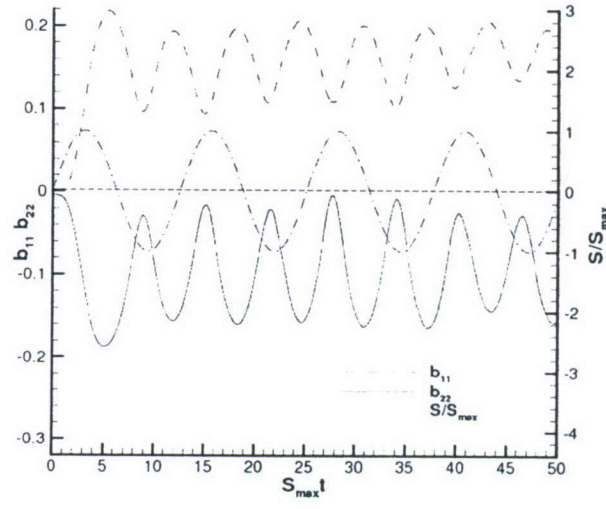


Figure 31: Evolution of b_{11} and b_{22} in $\omega/S_{max}=0.5$ case.

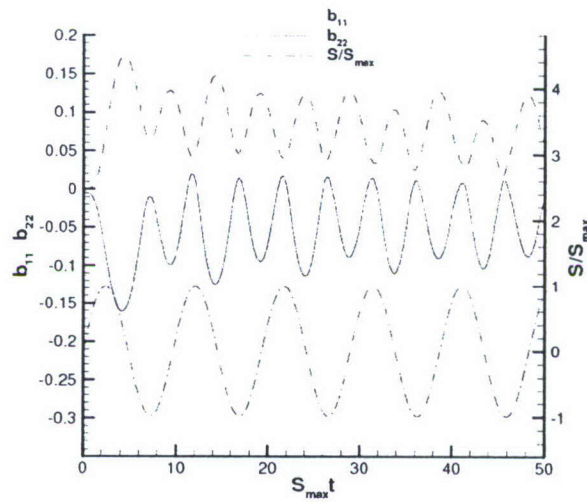


Figure 32: Evolution of b_{11} and b_{22} in $\omega/S_{\max} = 0.65$ case.

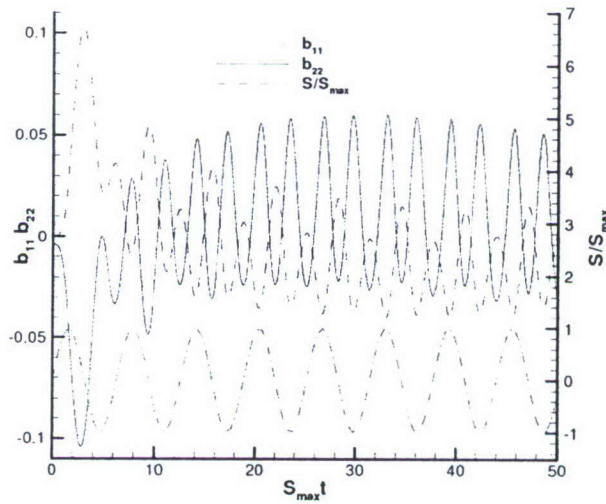


Figure 33: Evolution of b_{11} and b_{22} in $\omega/S_{\max} = 1.0$ case.

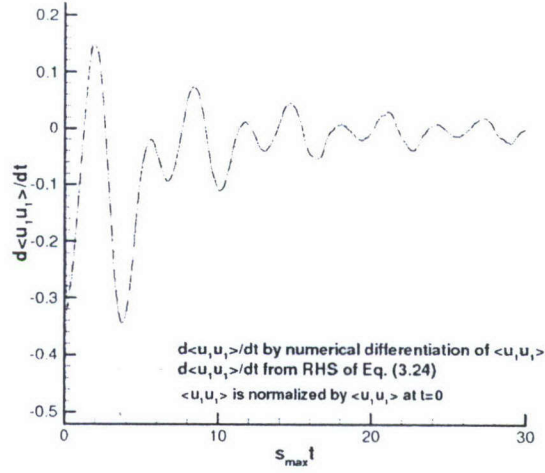


Figure 34: Comparison of $d\langle u_1 u_1 \rangle / dt$ computed from two different methods in $\omega/S_{max} = 1.0$ case.

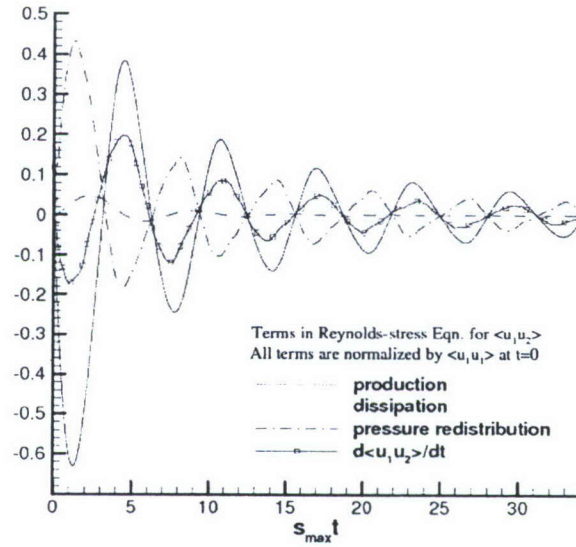


Figure 35: Temporal variation of $\langle u_1 u_2 \rangle$ budget in $\omega/S_{max} = 1.0$ case.

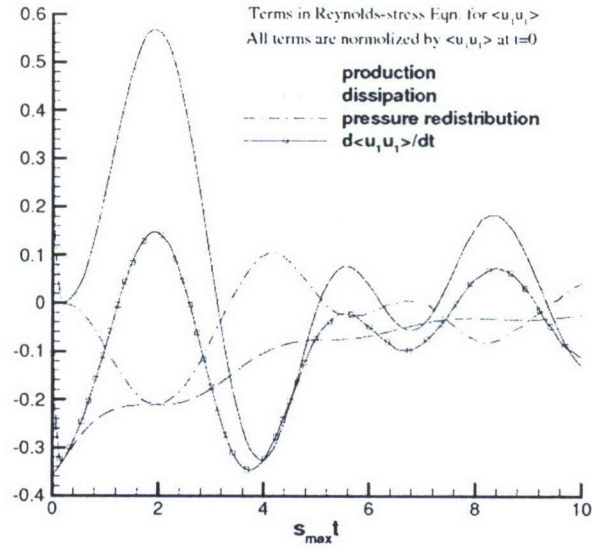


Figure 36: Early-time variation of $\langle u_1 u_1 \rangle$ budget in $\omega/S_{max} = 1.0$ case.

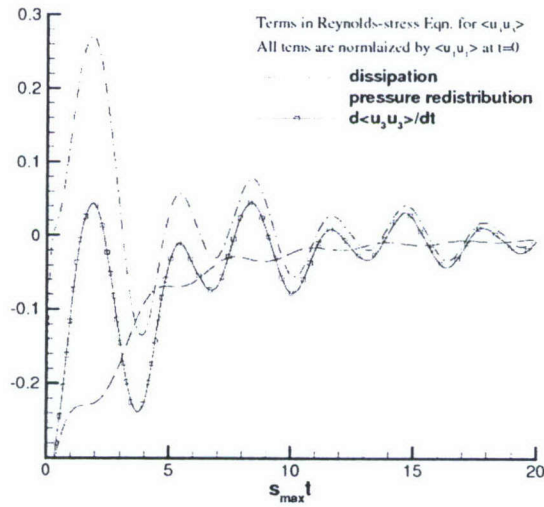


Figure 37: Early-time variation of $\langle u_3 u_3 \rangle$ budget at earlier stage in $\omega/S_{max} = 1.0$ case.

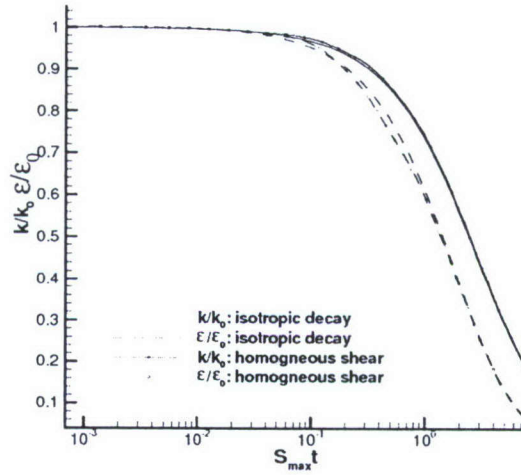


Figure 38: The evolutions of k and ε in isotropic decaying turbulence and homogeneous shear turbulence with $\omega/S_{max} = 10$.

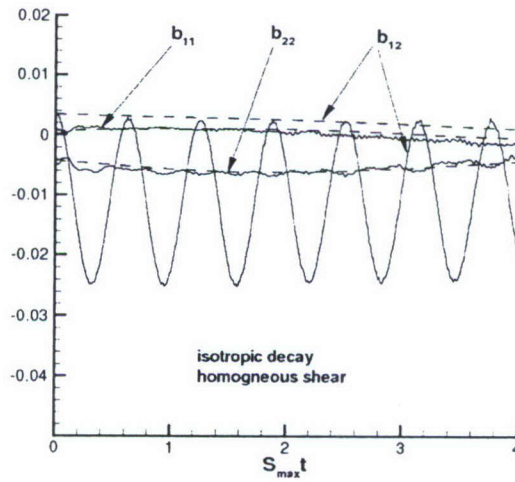


Figure 39: Evolution of anisotropy tensor in isotropic decaying turbulence and homogeneous shear turbulence with $\omega/S_{max} = 10$.

4 Unfinished problems.

We now describe the unfinished problems that were initiated during the last year of the work.

4.1 Near wall unsteadiness issues

Fan & Lakshminarayana [1] and Mankbadi & Mobark [2] consider unsteady boundary layers where either the wall or the free stream fluctuates. The flow is characterized by a near-wall flow that fluctuates in phase with the wall and an outer region with a substantial phase shift.

An instantaneous log-law does not in general exist and near-wall formulations based on the log-law and the equilibrium assumption are not appropriate according to Fan & Lakshminarayana. That disqualifies algebraic eddy-viscosity models and two-equation models with log-law boundary conditions or with near wall damping functions based on the wall friction (such as y^+). Moreover the existing low- Re K models are developed for steady flows and do not give satisfactory results for unsteady boundary layers.

Requirements on RANS models for highly unsteady turbulence. When the frequency of large-scale unsteadiness increases and approaches the turbulence characteristic frequency, turbulence is profoundly affected. That means that non-equilibrium effects become more pronounced. The very extreme kind of unsteady turbulence is rapidly distorted turbulence which has been thoroughly investigated in the first part of the study. It is reasonable to expect that turbulence models that are suited for non-equilibrium turbulence will perform well in unsteady turbulent flows as well. Some discussion in this regard can be found in Mankbadi & Mobark [2]. In keeping with the objectives of current research, we identify the following physical flow features as being crucial for successful RANS computation of unsteady wall-bounded flows:

1. The unsteady wall shear stress is out of phase with the flow away from the wall. Explicit corrections of the near wall influence cannot be based on the wall friction velocity u_τ . The local turbulent velocity scale \sqrt{K} may be an alternative and near-wall functions may be based on $R_y \equiv \sqrt{K}y/\nu$ or $R_t = K^2/\nu\epsilon$.
2. The near-wall unsteady region decreases in size for increasing frequencies and could be of the order of the viscous sub-layer. Correct and consistent near-wall asymptotic behavior is thus important for correct prediction of the mean wall shear stress. It is also important that the turbulence profiles are well reproduced through the buffer layer and thus models such as the Jones & Launder and the Wilcox standard $K - \omega$ models are not well suited due to the quite bad reproduction of the peak in the K -profile.
3. The prediction of boundary layer separation is important for capturing the unsteady flow around transonic airfoils. The eddy-viscosity assumption fails to correctly predict the production of the turbulent kinetic energy. That can instead be obtained by some *ad hoc* limitation of the production or eddy-viscosity but the same effect is obtained by using models based on full RST models.
4. When the frequency of the unsteadiness increases, the capability of the model to predict nonequilibrium turbulence increases in importance. That is not very well fulfilled by

standard eddy-viscosity two-equation models, but somewhat improved in e.g. the Menter SST $K - \omega$ model. Also here models based on full RST models are better suited for describing such flows.

Objective and approach. The main objective of this research is to seek physics-based modifications to current two-equation and second moment closure (SMC) models to improve their performance in unsteady flows. In such flows, the quasi-steady assumption will be inadequate. In this research period, we explored the effects of two important changes to the standard turbulence model paradigm. First and foremost, we recognize that spectral transfer rate and dissipation are not equal to one another in statistically unsteady turbulent flows. Given the nature of spectral energy cascade, it can be easily argued that dissipation lags behind cascade rate when the energy-containing range of the spectrum undergoes rapid changes. This has significant impact on the turbulence length scale equation and we propose a 2-equation length-scale model to account for these effects. This will have an impact on the current two-equation (which will become 3-equation) and SMC closures. An important inference from the above list of desirable features mentioned above and our previous DNS (direct numerical simulations) and RDT (rapid distortion theory) studies is that there could be a significant phase difference between the imposed mean velocity gradient (mean strain) and Reynolds stress. This is due to the fact that the Reynolds stress depends on the strain-rate history rather than the local mean strain rate. Thus, in our second investigation, we study the effect of introducing a phase lag between stress and strain in the Boussinesq constitutive relation. This work will only affect current two-equation models. This phase-lag can appear intrinsically in SMC models.

4.2 Two-equation length-scale model

The standard $K - \epsilon$ model is written as

$$\begin{aligned}\frac{DK}{Dt} &= P - \epsilon + D_K, \\ \frac{D\epsilon}{Dt} &= P_\epsilon - C_{\epsilon 2} \frac{\epsilon^2}{K} + D_\epsilon,\end{aligned}\tag{19}$$

where P_ϵ is the production of the dissipation ϵ . In the standard $K - \epsilon$ approach, the turbulence spectra is assumed to be in equilibrium, and, thus, P_ϵ may be directly related to P , the production of K

$$P_\epsilon = \frac{\epsilon P}{K}.\tag{20}$$

However, in non-equilibrium flows the ϵ equation should not immediately respond to a sudden change in production of K . Therefore, we propose to add relaxation to the production of ϵ by adding an additional transport equation for $s \equiv P_\epsilon$.

The resulting three-equation model may be written as

$$\begin{aligned}\frac{DK}{Dt} &= P - \epsilon + D_K, \\ \frac{D\epsilon}{Dt} &= s - C_{\epsilon 2} \frac{\epsilon^2}{K} + D_\epsilon,\end{aligned}$$

$$\frac{Ds}{Dt} = C_s \frac{\epsilon}{K} \left(C_{\epsilon 1} \frac{\epsilon P}{K} - s \right) + D_s. \quad (21)$$

At this stage, let us neglect the diffusion of s ($D_s = 0$). The relaxation time scale is proportional to the turbulent time scale K/ϵ with the relaxation proportionality constant C_s , being of order unity. This model will have the correct asymptotic behavior in homogeneous decaying turbulence. However, the asymptotic state in homogeneous developing flow will not be obtained. The reason is that the production of ϵ will not be constant at equilibrium. In order to obtain the correct asymptotic state, we may let s represent the production of ϵ normalized by K , and, thus, s becomes constant at the asymptotic state. The resulting three-equation model then becomes

$$\begin{aligned} \frac{DK}{Dt} &= P - \epsilon + D_K, \\ \frac{D\epsilon}{Dt} &= Ks - C_{\epsilon 2} \frac{\epsilon^2}{K} + D_\epsilon, \\ \frac{Ds}{Dt} &= C_s \frac{\epsilon}{K} \left(C_{\epsilon 1} \frac{\epsilon P}{K^2} - s \right) + D_s. \end{aligned} \quad (22)$$

In order to solve these equations in wall bounded flows we need some near-wall treatment. The Wilcox standard $K - \omega$ model is one of the preferred models, since it does not rely on friction velocity scaling. Let us transform equations (22) to a $K - \omega - s$ form, where ω is defined as

$$\omega = \frac{\epsilon}{\beta^* K}. \quad (23)$$

The transformed model reads

$$\begin{aligned} \frac{DK}{Dt} &= P - \beta^* \omega K + D_K, \\ \frac{D\omega}{Dt} &= \frac{s}{\beta^*} - \frac{\omega P}{K} - (C_{\epsilon 2} - 1) \beta^* \omega^2 + D_\omega, \\ \frac{Ds}{Dt} &= C_s \beta^* \omega \left(C_{\epsilon 1} \beta^* \frac{\omega P}{K} - s \right). \end{aligned} \quad (24)$$

The Wilcox $K - \omega$ model coefficients are related to the $K - \epsilon$ coefficients by the following:

$$\begin{aligned} \beta^* &\equiv C_\mu = 0.09 \rightarrow C_\mu = 0.09, \\ \alpha &\equiv (C_{\epsilon 1} - 1) = 0.556 \rightarrow C_{\epsilon 1} = 1.556, \\ \beta &= \beta^* (C_{\epsilon 2} - 1) = 0.075 \rightarrow C_{\epsilon 2} = 1.883. \end{aligned} \quad (25)$$

The author would like to further pursue this work in the future. (The three-equation model was developed in collaboration with Dr. Stefan Wallin of FOI/KTH, Sweden.)

4.3 Phase-lagged Boussinesq Approximation

As demonstrated in our previous papers (published previously under this project), in highly unsteady flows, Reynolds stress lags behind mean-flow strain. This is due to the fact that the

stress depends on the strain-rate history rendering the standard Boussinesq approximation invalid. We are currently investigating a model described by the following equations:

$$\begin{aligned}
\frac{dk}{dt} &= P - \epsilon, \\
\frac{d\epsilon}{dt} &= C_{e1} \frac{P \epsilon}{k} - C_{e2} \frac{\epsilon^2}{k}, \\
\langle u_i u_j \rangle &= \frac{2}{3} k \delta_{ij} - 2C_\mu \frac{k^2}{\epsilon} \bar{S}_{ij} \\
&= \frac{2}{3} k \delta_{ij} - 2C_\mu \frac{k^2}{\epsilon} S_{ij}(t - p), \\
P &= -\langle u_i u_j \rangle \frac{\partial \langle U_j \rangle}{\partial x_j} = 2\nu_T S_{ij}(t) S_{ij}(t - p).
\end{aligned} \tag{26}$$

In future work, the author will demonstrate this model possesses many important features that have not yet been fully exploited in current literature.

References

- [1] Fan, S. & Lakshminarayana 1993 Low-Reynolds-Number $K - \epsilon$ Model for Unsteady Turbulent Boundary-Layer Flows *AIAA J.* 31, 1777-1784.
- [2] Mankbadi, R.R. & Mobark, A. 1991 Quasi-steady turbulence modeling of unsteady flows *Int. J. Heat and Fluid Flow* 12, 122-129.
- [3] Jin, G. & Braza, M. 1994 Two-Equation Turbulence Model for Unsteady Separated Flows Around Airfoils *AIAA J.* 32, 2316-2320.
- [4] BHATNAGAR, P. L., GROSS, E. P. & KROOK, M. 1954 A model for collision processes in gases. I. Small amplitude processes in charged and neutral one-component system. *Phys. Rev. A* 94, 511-525.
- [5] CAMBON, C., SCOTT, J.F. 1999 Linear and Nonlinear Models of Anisotropic Turbulence. *Annu. Rev. Fluid Mech.* 31, 1-53.
- [6] CHAMPAGNE, F. H., HARRIS, V. G. & CORRSIN, S. 1970 Experiments on nearly homogeneous turbulent shear flow. *J. Fluid Mech.* 41, 81-139.
- [7] CHEN, H., CHEN, S. & MATTHAEUS, W. H. 1992 Recovery of the Navier-Stokes equations using a lattice-gas Boltzmann method. *Phys. Rev. A* 45, R5339-R5342.
- [8] DE SOUZA, F. A., NGUYEN, V. D. & TAVOULARIS, S. 1995 The Structure of highly Shear turbulence. *J. Fluid Mech.* 303, 155-167.
- [9] D'HUMIÉRES, D. 1992 Generalized lattice Boltzmann equations, In *Rarefied Gas Dynamics: Theory and Simulations*. ed. by Shizgal D. & Weaver D. P. *Prog. in Astro. Aero.* 159, 450-458.
- [10] D'HUMIÉRES, D., GINZBURG, I., KRAFCZYK, M., LALLEMAND, P., LUO, LI-SHI 2002 Multiple-relaxation-time lattice Boltzmann models in three dimensions. *Phil. Trans. R. Soc. Lond.* 360, 437-451.
- [11] GIRIMAJI, S. S. 2000 Pressure-strain correlation modeling of complex turbulent flows *J. Fluid Mech.* 422, 91-123.
- [12] GIRIMAJI, S. S., JEONG, E. & POROSEVA, S. V. 2003 Pressure-strain correlation in homogeneous anisotropic turbulence subject to rapid strain-dominated distortion. *Phys. of Fluids* 15, 3209-3222.
- [13] GUO, Z., ZHENG, C. & SHI, B. 2002 Discrete lattice effects on the forcing term in the lattice Boltzmann method. *Phys. Rev. E* 65, 046308.
- [14] HADZIC, I., HANJALIC, & K., LAURENCE, D. 2001 Modeling the response of turbulence subjected to cyclic irrotational strain. *Phys. Fluids* 13, 1739-1747.
- [15] HE, X. & LUO, LI-SHI 1997 Theory of the lattice Boltzmann equation: From Boltzmann equation to lattice Boltzmann equation. *Phys. Rev. E* 56, 6811-6817.

- [16] HIGUERA, F. J. & JEMENEZ, J. 1989 Boltzmann approach to lattice gas simulations. *Europhys. Lett.* **9**, 663–668.
- [17] JACOBITZ, F. G., SARKAR, S. & VAN ATTA, C. W. 1997 Direct numerical simulations of turbulence evolution in a uniformly sheared and stably stratified flow. *J. Fluid Mech.* **342**, 231–261.
- [18] KIDA S. & TANAKA M. 1994 Dynamics of vortical structures in homogeneous shear flow. *J. Fluid Mech.* **274**, 43–68.
- [19] KOELMAN, J. M. V. A. 1991 A simple lattice Boltzmann scheme for Navier-Stokes fluid flow. *Europhys. Lett.* **15**, 603–607.
- [20] LAUNDER, B. E., REECE, G. J. & RODI, W. 1975 Progress in the development of a Reynolds-stress turbulence closure. *J. Fluid Mech.* **68**, 537–566.
- [21] LEE, M. J., KIM, J. & MOIN, P. 1990 Structure of turbulence at high shear rate. *J. Fluid Mech.* **216**, 561–583.
- [22] MCNAMARA, G. & ZANETTI, G. 1988 Use of the Boltzmann equation to simulate lattice-gas automata. *Phys. Rev. Lett.* **61**, 2332–2335.
- [23] MEI, R., SHYY, W., YU, D. & LUO, LI-SHI 2000 Lattice Boltzmann method for 3-D flows with curved boundary. *J. Comp. Phys.* **161**, 680–699.
- [24] MOIN, P. & MAHESH, K. 1998 Direct numerical simulation: A tool in turbulence research. *Annu. Rev. Fluid Mech.* **30**, 539–578.
- [25] POPE, S. B. 2000 *Turbulent Flows*. Cambridge University Press, Cambridge.
- [26] QIAN, Y. H., D'HUMIÉRES D. & LALLEMAND, P. 1992 Lattice BGK models for Navier Stokes equation. *Europhys. Lett.* **17**, 479–484.
- [27] QUADRID, M. & SIBILLA, S. 2000 Numerical simulation of turbulent flow in a pipe oscillating around its axis. *J. Fluid Mech.* **424**, 217–241.
- [28] ROGALLO, R. S. 1981 Numerical experiments in homogeneous turbulence. *NASA TM-81315*.
- [29] ROGERS, M. M. 1986 The structure and modeling of the hydrodynamic and passive, scalar fields in homogeneous turbulent shear flow. PhD thesis, Department of Mechanical Engineering, Stanford University.
- [30] ROGERS, M. M. & MOIN, P. 1987 The structure of the vorticity field in homogeneous turbulent flows. *J. Fluid Mech.* **176**, 33–66.
- [31] SALHI, A. 2002 Similarities between rotation and stratification effects on homogeneous shear flow. *Theor. Comput. Fluid Dyn.* **15**, 339–358.

- [32] SALHI, A. & CAMBON, C. 1997 An analysis of rotating shear flow using linear theory and DNS and LES results. *J. Fluid Mech.* **347**, 171-195.
- [33] SALHI, A., CAMBON, C. & SPEZIALE, C. G. 1997 Linear stability analysis of plane quadratic flows in a rotating frame with applications to modeling. *Phys. Fluids* **9**, 2300-2309.
- [34] ROSE, W. G. 1996 Results of an attempt to generate a homogeneous turbulent shear flow. *J. Fluid Mech.* **25**, 97-120.
- [35] SCHUMACHER, J. & ECKHARDT, B. 2000 On statistically stationary homogeneous shear turbulence. *Europhys. Lett.* **52**, 627-632.
- [36] SPEZIALE, C. G., ABID, R. & BLAISDELL, G. A. 1996 On the consistency of Reynolds stress turbulence closures with hydrodynamic stability theory. *Phys. Fluids* **8**(3), 781-788.
- [37] SPEZIALE, C. G., GATSKI, T. B. & GIOLLA MHIRIS, N. M. 1990 A critical comparison of turbulence models for homogeneous shear flows in a rotating frame. *Phys. Fluids A* **2**, 1678-1684.
- [38] SPEZIALE, C. G., SARKAR, S. & GATSKI, T. B. 1991 Modeling the pressure-strain correlation of turbulence: an invariant dynamical system approach. *J. fluid Mech.* **227**, 245-272.
- [39] SUCCI, S. 2001 *The lattice Boltzmann equation for fluid dynamics and beyond*. Oxford University Press, New York.
- [40] TAVOULRIS, S. & CORRSIN, S. 1981a Experiments in nearly homogeneous turbulent shear flow with a uniform mean temperature gradient. Part 1. *J. Fluid Mech.* **104**, 311-349.
- [41] TAVOULRIS, S. & CORRSIN, S. 1981b Experiments in nearly homogeneous turbulent shear flow with a uniform mean temperature gradient. Part 2, the fine structure. *J. Fluid Mech.* **104**, 349-367.
- [42] TAVOULARIS, S. & KARNIK, U. 1989 Further experiments on evolution of turbulent stress and scales in uniformly sheared turbulence. *J. Fluid Mech.* **204**, 457-478.
- [43] TOWNSEND, A. A. 1976 *The Structure of Turbulent Shear Flow (2nd ed.)*. Cambridge University Press, Cambridge.
- [44] YU, D. & GIRIMAJI, S. S. DNS of homogeneous shear turbulence revisited with the lattice Boltzmann method. Accepted for publication in *Journal of Turbulence*.
- [45] YU, H., GIRIMAJI, S. S. & LUO, LI-SHI 2005 Lattice Boltzmann simulations of decaying homogeneous isotropic turbulence with and without system rotation. *Phys. Rev. E* **71**, 204501.
- [46] YU, H., GIRIMAJI, S. S. & LUO, LI-SHI DNS and LES of Decaying Isotropic Turbulence With and Without Frame Rotation. Accepted for publication in *Journal of Computational Physics*.

- [47] YU, D. MEI, R. LUO, LI-SHI & SHYY, W. 2003 Viscous flow computations with the method of lattice Boltzmann equation. *Prog. Aerospace Sci.* **39**(5), 329–367.